Full length article

Effect of non-stoichiometry on the crystal nucleation and growth in oxide glasses

Vladimir M. Fokin [a], Alexander S. Abyzov [b, c, *], Alisson M. Rodrigues [c],
Rogerio Z. Pompermayer [c], Guilherme S. Macena [a], Edgar D. Zanotto [c],
Eduardo B. Ferreira [a]

[a] São Carlos School of Engineering, University of São Paulo, São Carlos, Brazil
[b] National Science Center Kharkov Institute of Physics and Technology, Kharkov, Ukraine
[c] Department of Materials Engineering, Center for Research, Technology, and Education in Vitreous Materials, Federal University of São Carlos, São Carlos, Brazil

ABSTRACT

Non-stoichiometric glasses (NSG) are much more common than stoichiometric compositions. However, due to inherent difficulties, fundamental studies of crystallization kinetics of NSG are much less frequent. To shed light on the crystal nucleation and growth kinetics of NSG, we adopted a nucleation kinetics model, leaving the interfacial energy and diffusion coefficient as free parameters, to explain experimental nucleation data of glasses of three compositions in the pseudo-binary $Li_2O \cdot 2SiO_2 - BaO \cdot 2SiO_2$ model system. We show that, as the glass composition approaches the eutectic, the nucleation rates drop drastically, mainly due to an increase in the interfacial energy. This result corroborates the common empirical observation that eutectic compositions tend to show good glass-forming ability. We also found that the structural relaxation times are significantly shorter than the characteristic nucleation times, validating the widely used and scarcely tested assumption that relaxation does not play a noticeable role in crystal nucleation. For a stoichiometric glass the fitted diffusion coefficient determining nucleation, D, is lower than that determining the growth of macro crystals, D_U, and this difference significantly increases with decreasing temperature. On the other hand, the diffusion coefficient calculated from viscosity, D_η, is close to D_U at high temperatures and approaches D in the glass transition range. Finally, after crystallization of the primary phase (lithium disilicate), barium disilicate and more lithium disilicate crystals precipitate in the diffusion zone existing in the residual glass.

© 2019 Acta Materialia Inc. Published by Elsevier Ltd. All rights reserved.

1. Introduction

The composition of most glasses that undergo homogeneous internal crystal nucleation (in laboratory time scales) differs from those of the crystalline phases that precipitate out. This type of phase transformation is called non-stoichiometric crystallization. Despite the fact that non-stoichiometric crystallization is much more common in practice, due to inherent difficulties, fundamental studies of off-stoichiometric glasses are much scarcer than for stoichiometric crystallization. Deviation of the parent glass composition from that of the precipitated crystal phase results in a continuous change of the residual glass composition and significantly affects the nucleation kinetics and the overall course of crystallization. Hence the system properties, e.g., glass transition temperature [1,2] and electrical conductivity [3,4], also change. Considering the precipitation of only the primary crystalline phase, due to a delay in the formation of the secondary phases, the evolution of the residual glass composition can lead to a metastable equilibrium between the crystal and residual melt [1,5].

For a more in-depth understanding of *non-stoichiometric* crystallization kinetics, studies of simple glasses with compositions systematically moving away from the stoichiometry might be useful. However, to the best of our knowledge, only a few systematic investigations of this kind have been published, especially referring to nucleation rates, e.g. Refs. [6—13]. In the present paper, we use glasses having compositions of the pseudo-binary

* Corresponding author. National Science Center Kharkov Institute of Physics and Technology, Kharkov, Ukraine.
E-mail address: abyzov@kipt.kharkov.ua (A.S. Abyzov).

$Li_2O \cdot 2SiO_2 − BaO \cdot 2SiO_2$ join. We focus on the effect of the departure of the glass composition from the stoichiometry of the precipitated crystal phase on the nucleation rates. We also carried out growth rate determinations and compared the effective diffusion coefficients controlling nucleation, crystal growth, and viscous flow. We analyzed the nucleation kinetics for three glasses using a (time-dependent) *cluster distribution function* simulated in the framework of the kinetic model of nucleation [14—17].

2. Materials and methods

Twelve glasses with the composition $(100-X)Li_2O \cdot 2SiO_2 \cdot (X)$ $BaO \cdot 2SiO_2$ (hereafter referred to as BaX, where X is the molar percent of $BaO \cdot 2SiO_2$), listed in Table 1, were prepared as follows. The Ba0 glass was prepared from lithium carbonate and amorphous silicon oxide of analytical grade. The other glasses were synthesized from lithium carbonate (Alfa Aesar, USA, 99%), barium carbonate (Alfa Aesar, USA, 99.8%) and quartz powder with 20—30 μm particle granulometry (Vitrovita, Brazil, $\geq$ 99.9%). Melting of well-mixed reagents was performed in a platinum crucible for 2—3 h at 1400—1500 °C, depending on the glass composition. The melts were splat cooled between two steel plates to form glasses. The nominal batch compositions are listed in Table 1. As we will shown later, the nucleation rates drop dramatically when the glass composition approaches the eutectic. Therefore, only the glasses Ba0, Ba10, and Ba20 were used for the study of crystallization kinetics. An indirect confirmation of the proximity of the nominal composition of our glasses to the actual compositions is the coincidence of their liquidus temperatures with literature data for glasses with compositions that were confirmed by chemical analysis [18]. Based on the small variation in the crystal number density, N, calculated from several microstructural images obtained for each nucleation treatment, and since the nucleation rate strongly depends on the glass composition, we consider that our glasses are fairly homogeneous.

A differential scanning calorimeter (DSC 404, Netzsch, Selb/ Bavaria, Germany) with platinum pans and lids was used to determine the characteristic temperatures of the glasses: glass transition, T_g, solidus, T_S (below which only crystalline phases are in thermodynamic equilibrium), and liquidus, T_L (above which only the liquid is in equilibrium). The temperatures T_S and T_L were used to complete the phase diagram of the studied system.

The mass density, ρ, of the glasses was measured at room temperature by the Archimedes principle using a balance AX204 (Mettler Toledo).

The heat-treatments were performed in a vertical electric furnace with a pre-stabilized temperature within ± 1 °C. To estimate the number density, N, of crystals versus the nucleation time, t, at different nucleation temperatures, T_n, the well-known Tammann method or development method (e.g. Ref. [19]) was adopted, which consists of growing previously nucleated crystals at a development temperature $T_d > T_n$ up to a detectable size under a microscope. The nucleation rate, I, and growth rate, U, at the development temperature, T_d, must meet the following conditions: $I(T_d) \ll I(T_n)$ and $U(T_d) \gg U(T_n)$. Since the nucleation kinetics strongly slows down when the glass composition approaches the eutectic, for near-

eutectic compositions, we were forced to extend significantly the nucleation time, which reached several months for the Ba20 glass. Moreover, the complex crystal shapes limited the application of simple stereological equations for cubes, spheres, ellipsoids, plates or needles, to determine the volumetric number of nucleation sites from cross-section surfaces. Therefore, we mostly used thin plates (starting from 50-μm thickness) to estimate the total number of crystals in a given volume by transmission optical microscopy (Leica DMRX coupled with a Leica DFC490 CCD camera).

Both secondary electron (SE) and backscattered (BSE) electron imaging modes by scanning electron microscopy (SEM) (Inspect F50, FEI, Country) were used to study the crystal morphology and to reveal the "diffusion zones" next to them. The crystalline phase analyses were performed using an X-ray diffractometer (Ultima IV, Rigaku, Japan) with $CuK\alpha$ (1.5406 Å) incident radiation, operating at 20 mA and 40 kV.

3. Governing equations

Analyzing nucleation experiments requires the knowledge of the thermodynamic driving force for crystallization. The derivation of proper equations for non-stoichiometric crystallization is given below, based on an approach used in Ref. [20]. Moreover, a short description of simulations using a (time-dependent) *crystalline cluster size distribution*, $f(n, t)$, used for the analysis is also presented.

3.1. Thermodynamic driving force for non-stoichiometric crystallization

Consider a cluster of the new crystalline phase forming spontaneously within a supercooled melt at a constant temperature. The work of cluster formation, Eq. (1), has two parts: the first is negative due to the decrease in volume free-energy, and the second is positive due to interfacial free-energy [17]. A third term referring to the elastic strain energy can be neglected [21],

$$W_n = n\Delta\mu + K_s d_0^2 \sigma n^{\frac{2}{3}}. \tag{1}$$

Here, $\Delta\mu = \mu_s − \mu_l$ is the change of chemical potential during crystallization (the indexes "s" and "l" mean solid and liquid, respectively), σ is the nucleus/liquid interfacial energy, n is the number of "structural units" in the crystalline cluster, and d_0 is the characteristic size of the structural units, which is reasonably estimated as

$$d_0 \approx (V_M / N_A)^{1/3}, \tag{2}$$

where V_M is the crystal molar volume, and N_A is Avogadro's number. For our calculations, we use a typical value for the crystalline lithium disilicate, $d_0 = 0.48$ nm. We suppose that the clusters are spherical, for which the form factor, K_s, is

$$K_s = (36\pi)^{\frac{1}{3}}. \tag{3}$$

For regular solutions, the chemical potential for a particle in the liquid is given by Ref. [20]:

Table 1
Nominal batch compositions in mol%.

Glass	Ba0	Ba10	Ba20	Ba27	Ba30	Ba34	Ba37	Ba50	Ba60	Ba47	Ba85	Ba100
$Li_2O \cdot 2SiO_2$	100	90	80	73	70	66	63	50	40	25	15	0
$BaO \cdot 2SiO_2$	0	10	20	27	30	34	37	50	60	75	85	100

$$\mu_l = \mu_l^0 + k_B T \ln(1 - x) + \alpha_l(x), \tag{4}$$

where x is the molar fraction of the second component ($x = X/100$), which is barium disilicate in this case, k_B the Boltzmann constant, and $\alpha_l(x)$ is a function only of x and not of temperature.

For particles in a crystal phase emergent in the supercooled liquid of the same composition (in this case, lithium disilicate), $x = 0$ and $\alpha_s(0) = 0$, and

$$\mu_s = \mu_s^0. \tag{5}$$

Hence, we have

$$-\Delta\mu = \mu_l^0 - \mu_s^0 + k_B T \ln(1 - x) + \alpha_l(x). \tag{6}$$

For $x = 0$,

$$\mu_l^0 - \mu_s^0 = d_0^3 \Delta G_V^0(T), \tag{7}$$

where $\Delta G_V^0(T)$ is the thermodynamic driving force for crystallization of the stoichiometric composition ($x = 0$), so that

$$\Delta G_V(x) = \frac{-\Delta\mu}{d_0^3} = \Delta G_V^0(T) + \frac{k_B T}{d_0^3} \ln(1 - x) + \frac{\alpha_l(x)}{d_0^3}. \tag{8}$$

Recall that at $T = T_L(x)$, $\Delta\mu = 0$, therefore

$$\Delta G_V^0(T_L) + \frac{k_B T_L(x)}{d_0^3} \ln(1 - x) + \frac{\alpha_l(x)}{d_0^3} = 0. \tag{9}$$

With Eq. (9), we can obtain the $T_L(x)$ dependence or function $\alpha_l(x)$ when $T_L(x)$ is known. Eqs. (8) and (9) yield an expression for the thermodynamic driving force as a function of temperature and composition,

$$\Delta G_V(T, x) = \Delta G_V^0(T) - \Delta G_V^0(T_L(x)) + \frac{k_B(T - T_L(x))}{d_0^3} \ln(1 - x). \tag{10}$$

Thus, to determine the thermodynamic driving force of crystallization of a non-stoichiometric glass ($x > 0$), it is only necessary to know the liquidus temperature, $T_L(x)$, and $\Delta G_V^0(T)$ for a crystalline phase evolving in a liquid of stoichiometric composition ($x = 0$). In the present work, we used data of Takahashi and Yoshio [22], which were obtained using formal thermodynamics and experimental calorimetric data on the heat of melting and specific heat capacities of lithium disilicate glass and crystal as a function of temperature. Their results lay between the Turnbull and the Hofmann approximations, as expected (see, e.g., Appendix in Ref. [19]). For convenience, we used the polynomial expression given by Eq. (11), which adequately fits the Takahashi & Yoshio data:

$$\Delta G_V^0(T) = 8.40245024 \cdot 10^8 - 540266 \cdot T - 78.5116 \cdot T^2 \; [J \cdot m^{-3}] \tag{11}$$

For the dependence of the liquidus temperature, $T_L(x)$, on the molar fraction of barium disilicate, x, (Fig. 4a), we used the following polynomial fit:

$$T_L(x) = \begin{cases} 1307 - 119.05 \cdot x - 384.4 \cdot x^2, & x \leq 0.373 \\ 1684 - 572.46(1 - x) - 295.3(1 - x)^2, & x > 0.373 \end{cases} \tag{12}$$

Fig. 1 shows the calculated thermodynamic driving force for the crystallization of glasses with different chemical compositions as a
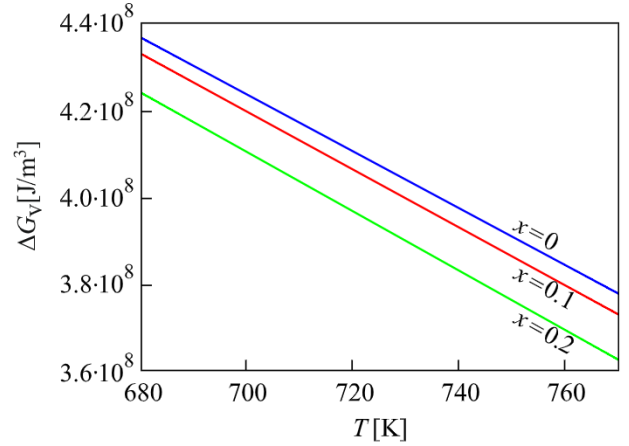

Fig. 1. Calculated thermodynamic driving force, $\Delta G_V(T)$, for compositions in the $Li_2O \cdot 2SiO_2 - BaO \cdot 2SiO_2$ system, with different $BaO \cdot 2SiO_2$ molar fractions, x.

function of temperature.

3.2. Numerical simulation

The work of cluster formation, W_n, reaches a maximum value at the critical size, n^* [14,23],

$$n^* = \frac{32\pi}{3} \left(\frac{\sigma}{d_0 \Delta G_V} \right)^3 \tag{13}$$

Clusters larger than n^* will grow, whereas the smaller ones will shrink. The (time-dependent) cluster distribution function, f_n, is obtained from a set of coupled linear differential equations [14–17,25],

$$\frac{df_n}{dt} = \omega_{n-1,n}^+ f_{n-1} + \omega_{n+1,n}^- f_{n+1} - \left(\omega_{n,n+1}^+ + \omega_{n,n-1}^- \right) f_n, \tag{14}$$

where ω^+ and ω^- are the attachment and detachment rates [25],

$$\omega_{n-1,n}^+ = K_s \frac{n^{2/3}}{d_0^2} D \begin{cases} 1 & \text{if } n \geq n^* \\ \exp\left(-\frac{W_n - W_{n-1}}{k_B T} \right) & \text{if } n < n^* \end{cases}, \tag{15}$$

$$\omega_{n+1,n}^- = \omega_{n-1,n}^+ \exp\left(\frac{W_n - W_{n-1}}{k_B T} \right). \tag{16}$$

At the time nucleation reaches the steady-state regime with 99.9% tolerance, the distribution function $f(n_1, t) < 1 \, m^{-3}$ at $n_1 > 2569$, 2522, and 2893 for Ba0, Ba10, and Ba20, respectively, for all considered nucleation temperatures. Thus, we used a maximal crystal size given by $n_{max} = 10,000$, which is enough to reach the steady-state nucleation regime. To solve Eq. (14) at the boundary $n = n_{max}$, we used the Taylor expansion for the distribution function, $f(n_{max} + 1, t) = 2f(n_{max}, t) - f(n_{max} - 1, t)$.

At $t = 0$, we assumed the cluster size distribution is equal to the equilibrium distribution of heterophase fluctuations in the liquid at T_L [26],

$$f_n(0) = d_0^{-3} \exp\left(-\frac{W_n - W_1}{k_B T_L} \right), \tag{17}$$

where W_n is determined by Eq (1).

To compute the steady-state nucleation rates, I_{st}, and the respective induction times for nucleation, we used the effective

diffusivity controlling nucleation, $D(T)$, and interfacial energy, $\sigma(T)$, as fitting parameters to the N versus *time* experimental data (see Fig. 8 and Figs. A1, A2 in Appendix).

As an example, the calculated cluster size distribution, f_n, for the Ba20 glass after different time periods at 415 °C is shown in Fig. 2.

From the calculated cluster size distribution at a nucleation temperature, T_n, we obtain the number of crystal nuclei as a function of time,

$$N_n(t) = \sum_{n^*(T_n)}^{\infty} f_n, \tag{18}$$

and after development at a temperature T_d,

$$N_d(t) = \sum_{n^*(T_d)}^{\infty} f_n. \tag{19}$$

These calculations assume an infinitely high heating rate from T_n to T_d.

4. Results and discussion

4.1. Phase diagram and glass properties

The liquidus temperatures are needed to calculate the driving force for crystallization of non-stoichiometric compositions. The $Li_2O \cdot 2SiO_2 - BaO \cdot 2SiO_2$ equilibrium diagram was completed here using the solidus and liquidus temperatures obtained from DSC curves (e.g., Fig. 3), and is shown in Fig. 4a. This diagram reveals a single eutectic point at 37 ± 2 mol% $BaO \cdot 2SiO_2$. The position of this eutectic was confirmed by the so-called "Tammann triangle," which is obtained by plotting the area of the DSC eutectic melting peak as a function of composition and reaches the maximum at the eutectic composition (Fig. 4b). Our data for T_L are in good agreement with the literature data (Fig. 4a), confirming the agreement between the actual and the nominal glass compositions.

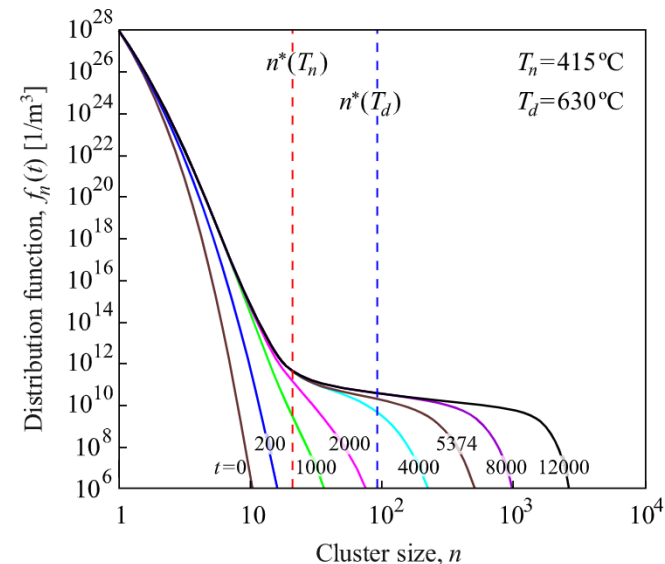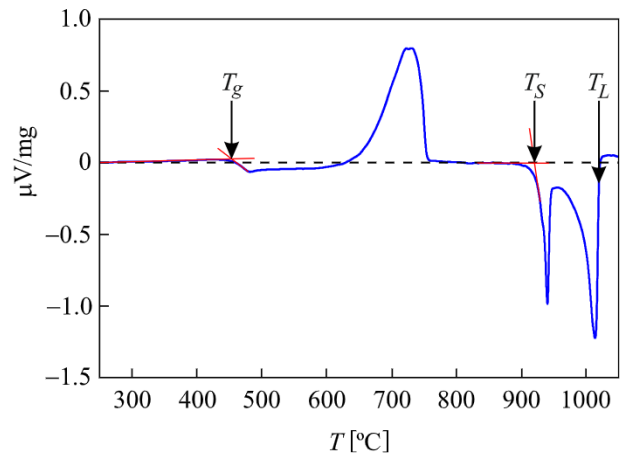The glass transition temperature monotonically increases with

Fig. 3. DSC trace for a piece of glass of 25 mg. Heating rate = 10 °C/min.

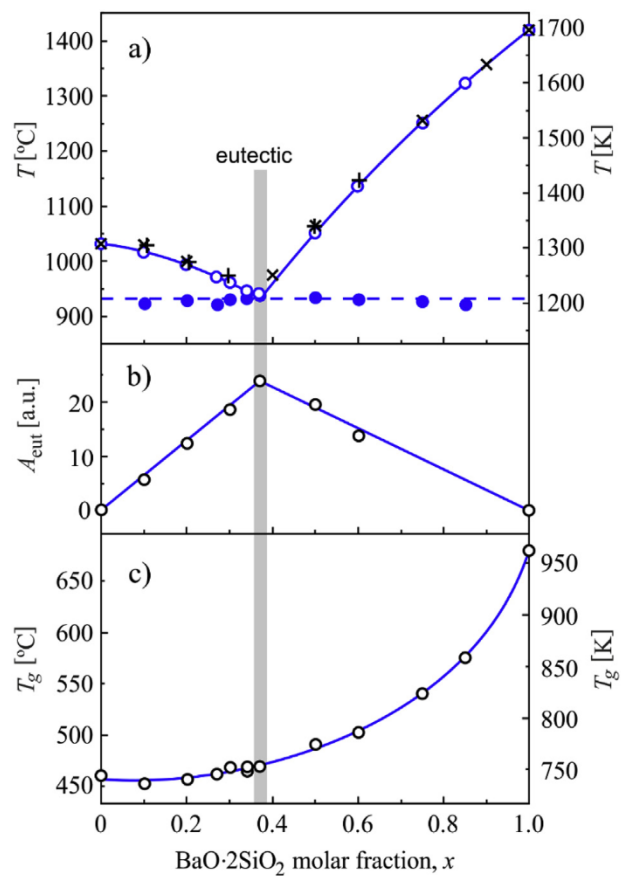

Fig. 4. a) Dependence of the liquidus, $T_L(x)$, and solidus, $T_S(x)$, temperatures on the $BaO \cdot 2SiO_2$ molar fraction. Points – this work, crosses (+ and ×) are from Refs. [9,18], respectively, the solid line is plotted according to Eq. (12). b) Area of the eutectic melting peak, A_{eut}, versus composition (Tammann triangle). c) Glass transition temperature, $T_g(x)$ versus $BaO \cdot 2SiO_2$ molar fraction (points – this work; the line is only a guide for the eyes).

Fig. 2. Calculated *cluster size distribution*, f_n, for the Ba20 composition at $T_n = 415$ °C for different time periods (hours). Red and blue vertical lines show the critical sizes at the nucleation and development temperatures, correspondingly. The steady-state regime, i.e., $f_{n'}(t) \approx$ const. is reached after approximately 8000 h at the development temperature. (For interpretation of the references to colour in this figure legend, the reader is referred to the Web version of this article.)

$BaO \cdot 2SiO_2$ content and does not show any peculiarity in the eutectic point (Fig. 4c). The glass density also increases with increasing content of barium disilicate, however, in contrast to the glass transition temperature, beginning with the eutectic composition, the increase in density takes place at a lower rate after the eutectic composition (Fig. 5a). The linear dependence of density on
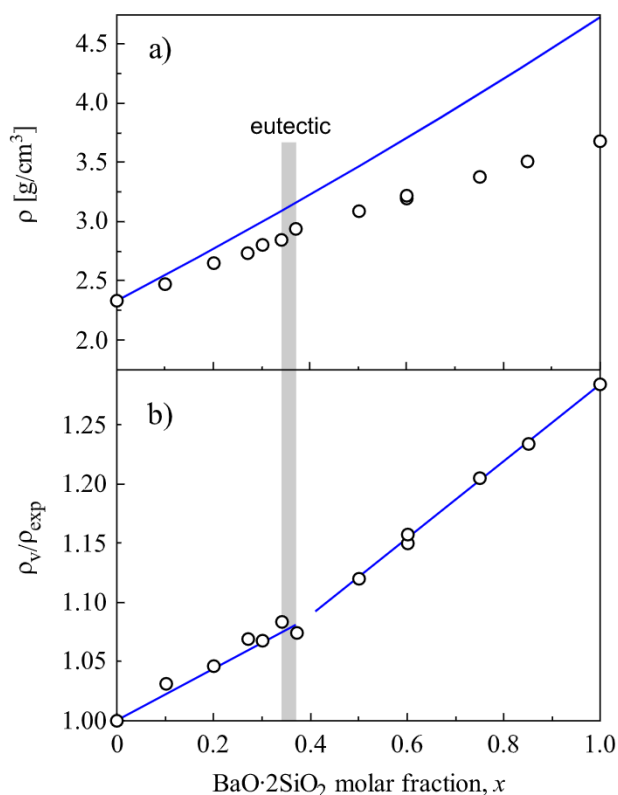
Fig. 5. Dependence of a) glass density, ρ, (points − experimental data ρ_{exp}, line − density ρ_V calculated at the condition of constant molar volume) and b) ratio ρ_V / ρ_{exp} on the BaO·2SiO$_2$ molar fraction, x.

Fig. 6. a) Reflected light optical micrograph of a cross-section in a Ba10 glass sample after nucleation at $T_n = 462\,°C$ for 72 h and development at $T_d = 630\,°C$ for 6 min. b) Transmitted light optical microscopy image of a 0.42 mm thick plate of a Ba20 glass after nucleation at $T_n = 460\,°C$ for 242 h and development at $T_d = 630\,°C$ for 20 min.

composition with a slope change at the eutectic point is more noticeable in Fig. 5b, which shows the ratio of the density calculated assuming a constant molar volume to the experimental density, ρ_V / ρ_{exp}. This dependence reflects an increase in the molar volume due to the replacement of lithium by barium, which takes place faster after the eutectic composition.

4.2. Crystallization kinetics

Fig. 6 shows optical micrographs of the Ba10 and Ba20 glasses after nucleation and development heat-treatments, as examples.

According to X-ray analysis, in the case of the Ba10 sample, the crystal phase developed for short treatment periods is lithium disilicate, whereas, for the Ba20 sample, traces of barium disilicate are also detected (Fig. 7). This result is expected since lithium disilicate is the primary phase for the three glasses (Ba0, Ba10, and Ba20) used here to measure nucleation rates (Fig. 4). By increasing the development time, a small amount of barium disilicate also appears in glass Ba10. The formation of the BaO·2SiO$_2$ crystals will be commented on later.

4.2.1. Crystal nucleation

The number density, $N(t)$, of lithium disilicate crystals as a function of nucleation time are shown in Fig. 8a−c for different temperatures and glasses. Similar plots for other temperatures are shown in the Appendix, Figs. A1 and A2.

The dashed-dotted lines in Fig. 8a−c shows $N(t)$ curves calculated by Eq. (18) considering only the nucleation treatment, and the solid lines calculated by Eq. (19) taking into account the development treatment. The dashed lines show the asymptotes used to calculate the steady-state nucleation rates, I_{st}, arrows show
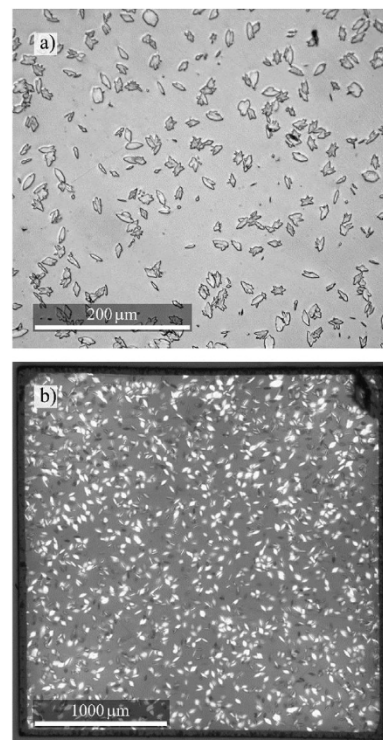
induction times for nucleation, $t_{ind,n}$, and after development, $t_{ind,d}$. It should be noted that the steady-state nucleation rates calculated from the $N(t)$ curves after nucleation are equal to those obtained directly from the experimental $N(t)$ data after development, and therefore we did not distinguish them. Fig. 8d−f shows the I/I_{st} ratios for the three glass compositions, where the vertical dashed lines mark the time at $I/I_{st} = 0.9$ and the maximum experimental nucleation time, t_{max}.

The fitted curves are close to the experimental points at advanced stages of nucleation. However, in the beginning, before the steady-state is established, the experimentally measured values are always higher than the calculated values. This divergence is likely due to one or more of several reasons:

i) the finite cooling rate during the quenching procedure to form a glass leads to (some) crystal nucleation when the sample temperature span into the temperature interval of maximum nucleation rate, T_{max} [27];

ii) some nucleation might also happen on the heating path from the nucleation to the growth temperature, which depends on the nucleation rates and heating rate [27]. The origin of this effect and (i) are the same, i.e., additional nucleation when the temperature crosses the T_{max} region.

These problems are beyond the scope of this paper. A third possibility, a possible influence of the structural relaxation process, is still under investigation and will be partially tackled in this article.

According to Fig. 8, the maximum time of the nucleation experiments, t_{max}, exceeds the time for establishing the steady-state nucleation rate, $I_{st}(T_n)$, i.e., the time for the number density of critical-sized clusters, $n^*(T_n)$, to reach a stationary value. For glasses

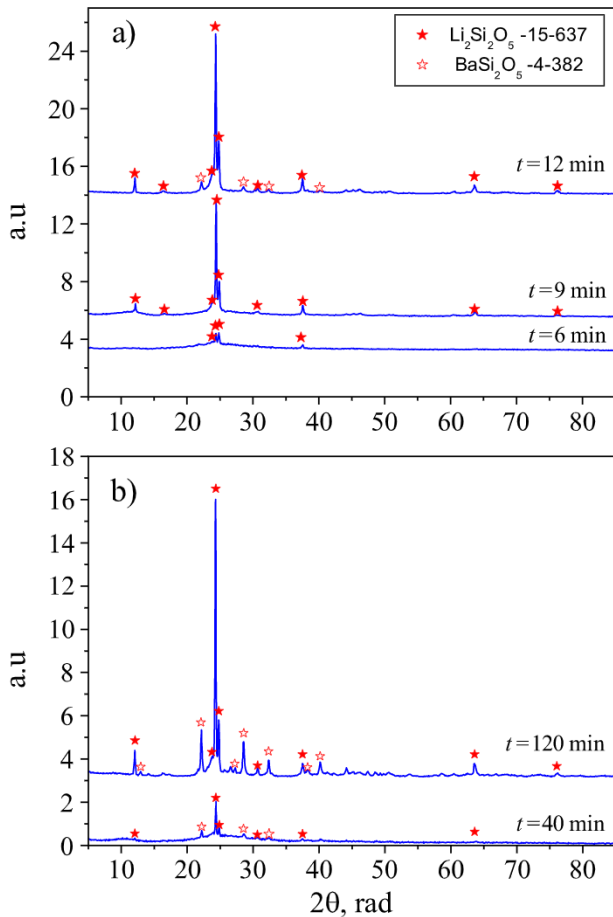**Fig. 7.** X-ray diffraction patterns of glasses Ba10 (a) and Ba20 (b) after nucleation at $T_n = 460\,°C$ for 72 h and development at $T_d = 630\,°C$ for different times indicated in the figures.

Ba0 and Ba10 (Fig. 8d and e), t_{max} also exceeds the time to reach the stationary regime for clusters of the critical size at the development temperature, $n^*(T_d)$. For the Ba20 glass, t_{max} is not enough for the number density of clusters of size $n^*(T_d)$ to reach its stationary value (Fig. 8f). In this case, the nucleation rate evaluated from the experimental $N(t)$ reached only approximately 60% of its steady-state value. To achieve a steady-state, we should extend the evaluation of $N(t)$ from 7 to 9 months. However, with the *cluster nucleation model,* one can estimate the steady-state nucleation rate. The nucleation temperature $T_n = 415\,°C$ for Ba20 glass is $40- 50\,°C$ below the glass transition temperature estimated by DSC for the splat cooled and annealed glasses, namely, $454\,°C$ and $462\,°C$, respectively.

The crystal cluster/liquid interfacial energy, σ, and diffusion coefficient, D, were used as fitting parameters to experimental values at each temperature, and are given in the Appendix, Tables A1 and A2 for glasses Ba10, and Ba20.

Note that, in this way, $\sigma(T,x)$ is temperature dependent and, to a first approximation, for temperatures above the maximum nucleation rates, T_{max}, it can be fitted by a linear function:

$$\sigma(T,x) = 0.1196 - 0.1435x + 0.825x^2 + 10^{-4}\left(0.694 + 2.083x\right.$$
$$\left. - 11.11x^2\right)T \quad \left[J/m^2\right].$$
(20)

It has been suggested that the linear dependence of the

interfacial free energy on temperature is a consequence of the diffuse interface between the nucleating cluster and the parent supercooled liquid, which is considered in the "diffuse-interface" theory [28–30] (see detailed discussion in Ref. [31], Chapter 4, Sections 3). However, the use of such an advance over the CNT theory ([31], Chapter 4, Sections 4) for the analysis of experimental data is difficult because the problem becomes two-dimensional, since the second independent variable (which is related to the diffusivity of the boundary) is added to the cluster size.

Therefore, in this article we use the CNT framework. To facilitate the data analysis, we used a fitting function, $D(T,x)$, in Arrhenius form with composition-dependent coefficients,

$$D(T,x) = D_0(x)\exp\left[- 62,700(1 + 0.2x)T^{-1}\right],$$
(21)

where

$$D_0(x) = 2.2 \cdot 10^{15}\exp\left(11.18x - 29x^2\right) \quad \left[m^2/s\right].$$

The pre-exponential therm, $D_0(x)$, grows weakly with x. However, owing to the growth of diffusion activation energy, the diffusion coefficient Eq. (21) decreases with x.

In this way, the temperature dependencies of D and σ are shown in Fig. 9 for glasses Ba0, Ba10, and Ba20.

Fig. 10 shows the steady-state nucleation rate as a function of temperature for Ba0 ($x = 0$), Ba10 ($x = 0.1$), and Ba20 ($x = 0.2$) glasses. The experimental values of the nucleation rate at low temperatures depart more and more from the computed values using the linear temperature dependence of specific surface energy, σ. This old unresolved problem was discussed in detail in Refs. [21,32–34] and is beyond the scope of this paper.

According to Fig. 10, the deviation of the glass from the stoichiometric lithium disilicate ($x = 0$) towards the eutectic composition results in a slight decrease in the temperature of the steady-state nucleation rate maximum, T_{max}, and a significant drop (about three orders of magnitude) of its intensity, $I_{st}(T_{max})$. A similar trend is observed for the nucleation rate computed with a linear dependence of $\sigma(T)$ (dashed curves in Fig. 10). The decrease in $I_{st}(T_{max})$ correlates with an increase in the reduced glass transition temperature $T_{gr} = T_g/T_L$, where T_L is the liquidus temperature determined by Eq. (12). This behavior agrees with a well-known trend: the higher T_{gr}, the lower the steady-state nucleation rate maximum, shown in Fig. 11 for different silicate glasses and the three glasses studied here: Ba0 ($x = 0$), Ba10 ($x = 0.1$), and Ba20 ($x = 0.2$).

As stated before, this work focuses on the effect of the deviation of the glass composition from stoichiometry on the crystallization kinetics. According to CNT, the magnitude and temperature dependence of the nucleation rate are mainly determined by the diffusion coefficient, D, and the thermodynamic barrier, W_{n^*}, whereas the crystal growth rate at deep undercooling is determined in practice only by the diffusion coefficient.

To help the analysis of the nucleation rates given in Fig. 10, the driving force of crystallization, ΔG_V, the surface energy, σ, the thermodynamic barrier W_{n^*}, and the diffusion coefficient, D, are summarized in Fig. 12 (a) to (d), respectively, as functions of the glass composition, x.

As the difference between glass and crystal compositions increases, the increase of $\sigma(x)$ and decrease of $\Delta G_V(x)$ increase the thermodynamic barrier for nucleation. Together with a decreasing diffusion coefficient, these variations lead to a significant drop in the nucleation rate. To separate the effects of the thermodynamic and kinetic barriers, we compare them at $T_n = 730$ K. If only the thermodynamic barrier changed, the nucleation rate would be
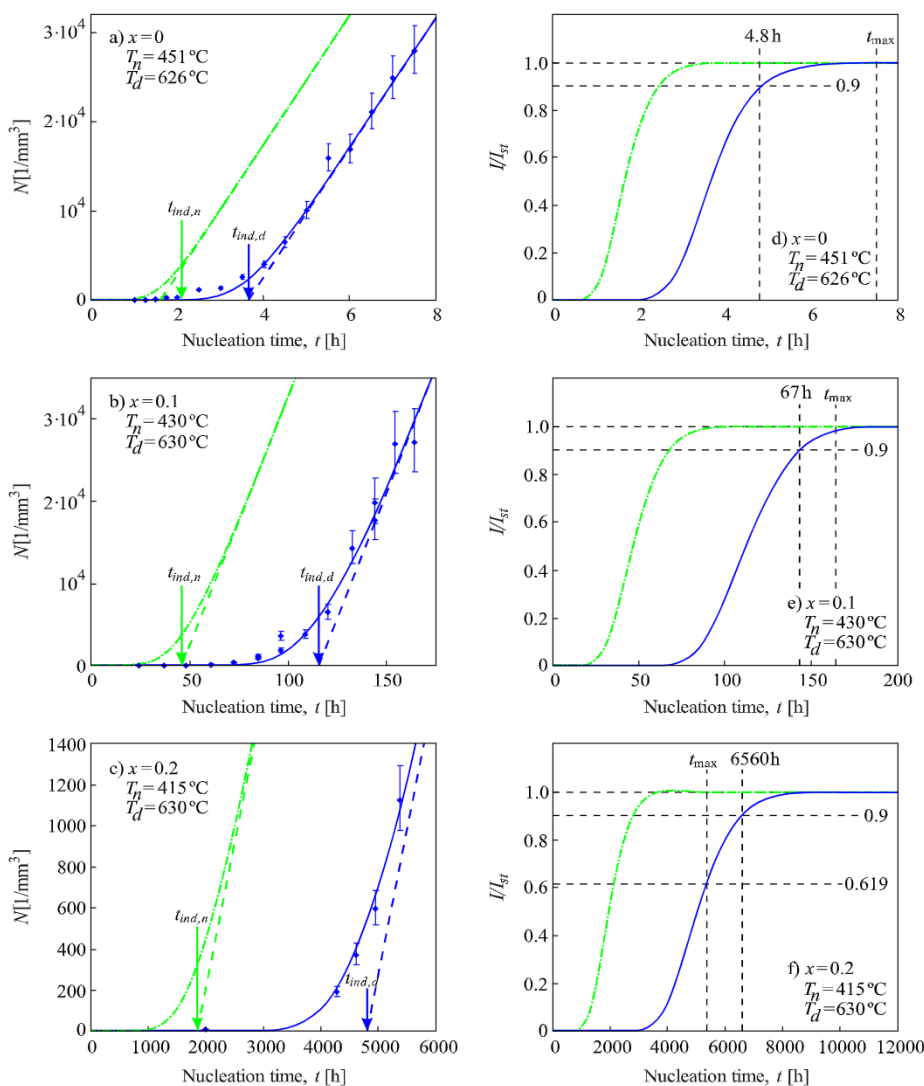
Fig. 8. (a–c) $N(t)$ curves for glasses with different $BaO \cdot 2SiO_2$ molar fractions: a) $x = 0$, b) $x = 0.1$ and c) $x = 0.2$. The dashed-dotted lines were calculated by Eq. (18) considering only the nucleation treatment and the solid lines are curves given by Eq. (19) fitted to the experimental data points after the development treatment. The dashed lines show the asymptotes used to calculate the steady-state nucleation rate, I_{st}; the arrows show the induction times for nucleation, $t_{ind,n}$, and after development, $t_{ind,d}$. Figures (d–f) show the I/I_{st} ratios for the same glasses. The vertical dashed lines mark the time when $I/I_{st} = 0.9$ and the maximum experimental nucleation time, t_{max}. The experimental data for Ba0 are from Ref. [24], and for Ba10 and Ba20 refer to this work.

reduced by more than 200 times, while changing only the diffusion coefficient would lead to a 10-fold decrease in the nucleation rate. When only the thermodynamic barrier increases, at a fixed kinetic barrier, the temperature of nucleation rate maximum shifts toward lower temperatures (e.g. Ref. [19]). In our case, the kinetic barrier changes slightly, leading to a small shift of T_{max} towards low temperatures.

The effect of glass composition on the crystal nucleation rate results from the interplay between the changes of the thermodynamic and kinetic barriers, and this effect is dependent on the properties of the system under consideration. Nevertheless, one can expect an increase in surface energy when the glass composition deviates from that of the precipitated crystals.

4.2.2. Structural relaxation versus nucleation

To shed light on the very fundamental question of whether structural relaxation affects the nucleation process, we measured how the glass transition temperature changes during the nucleation treatment (Fig. 13). It follows from Fig. 13 that T_g increases for

both, the splat-cooled and the annealed, glasses (as expected), reaching the same constant value after approximately 3–4 days at 415 °C. This time is *much lower* than the characteristic nucleation times. The experimental induction time after development is $t_{ind,d} = 200$ days. From the simulations, the intrinsic induction period for nucleation $t_{ind,n} = 77$ days. Most importantly, the time t_1 to form the *first* critical nucleus is approximately **25** days for a typical laboratory sample of 10 mm^3 (Fig. A3 in the Appendix). Thus, we can conclude that nucleation at the discussed temperature occurs long *after* relaxation, in the (metastable) supercooled liquid state, and is hardly disturbed by the structural relaxation process. These interesting, relevant results require a more in-depth study with other glasses at different temperatures and are beyond the scope of this article.

4.2.3. Crystal growth

To estimate the diffusion coefficient, D_U, from experimental crystal growth rates, we used the simple *normal growth model* (e.g. Ref. [36]), which yields
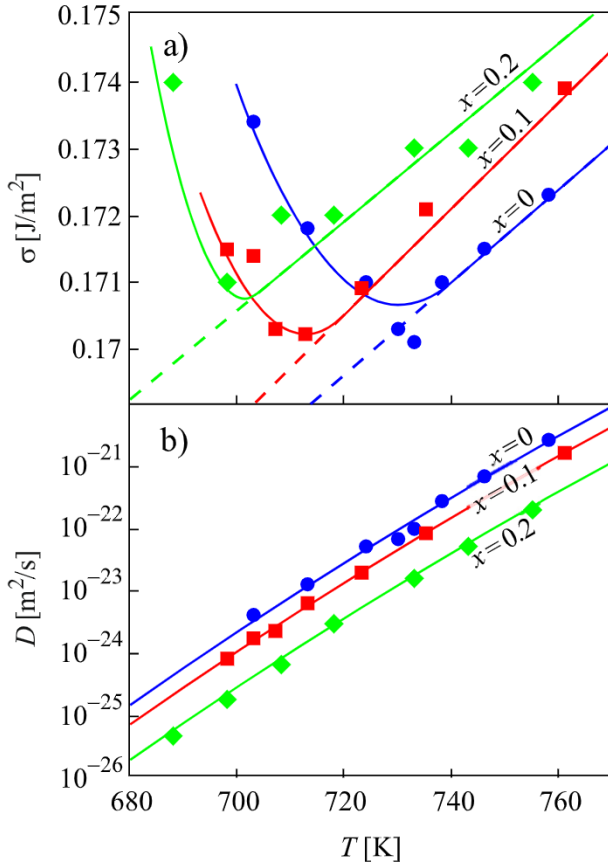
Fig. 9. a) Interfacial energy for Ba0 (x = 0), Ba10 (x = 0.1), and Ba20 (x = 0.2) as a function of temperature. The points were estimated as fit parameters of $N(t)$ given by Eq. (19) for experimental data at each temperature, whereas the dashed lines were plotted considering a linear $\sigma(T)$, Eq. (20), on fitting. The solid lines were calculated assuming the deviation of $\sigma(T)$ from the linear approximation. b) Diffusion coefficient as a function of temperature; the points were estimated as fit parameters from the $N(t)$ curves; the solid lines show Arrhenius dependencies according to Eq. (21).
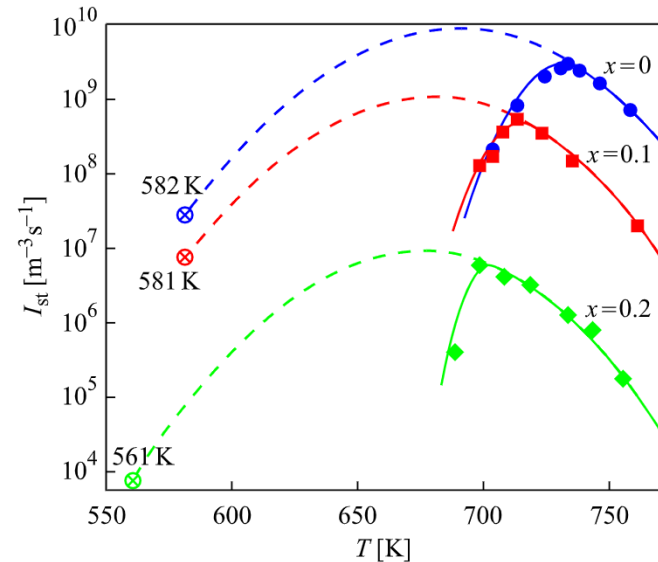
Fig. 10. Steady-state nucleation rates, $I_{st}(T)$, computed from $N(t)$ curves for different temperatures and BaO·2SiO$_2$ molar fractions, x. The dashed lines were calculated from fitting $N(t)$, Eq. (19), with a linear $\sigma(T)$ given by Eq. (20). The solid lines were calculated using the fitted values of $\sigma(T)$ above and below T_{max} (see Fig. 9a). Below the temperatures marked by ⊗, the critical size from Eq. (13) becomes < 10, and then CNT is expected to lose validity.
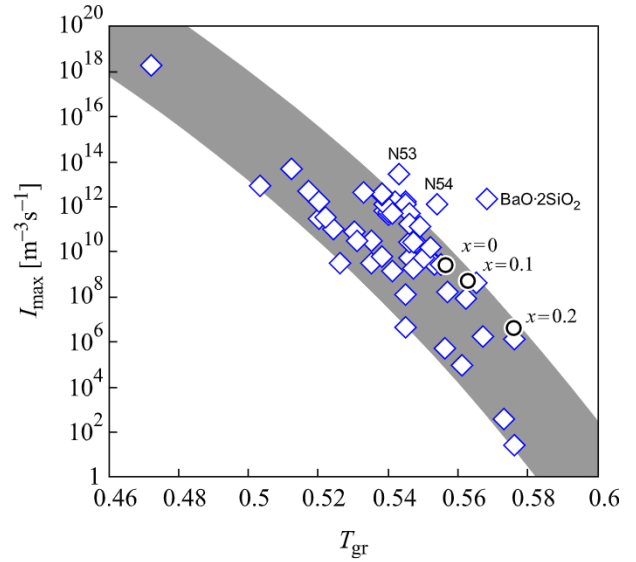

Fig. 11. Steady-state nucleation rate maximum versus reduced glass transition temperature for several stoichiometric and non-stoichiometric silicate glasses that show homogeneous nucleation [35]. The circles added here correspond to the glasses Ba0 (x = 0), Ba10 (x = 0.1), and Ba20 (x = 0.2).

$$U = \frac{D_U}{d_0} \qquad (22)$$

at deep undercooling, as in our case. The crystal growth rate was estimated by the equation

$$U = \frac{1}{2}\frac{dH}{dt}. \qquad (23)$$

considering the time-dependence of the maximal size of the crystals, H, (see, e.g., Fig. 14).

The experimental crystal growth rates, $U(T)$, are shown in Tables A3 and A4 in the Appendix. The diffusion coefficients estimated from the crystal growth rates via Eq. (22), D_U, are shown in Fig. 15 as a function of temperature for glasses Ba0, Ba10, and Ba20. For the sake of comparison, we also replot the diffusion coefficients, D, already shown in Fig. 10, that govern the formation of crystalline clusters of nanoscale sizes, including clusters of critical size.

Fig. 15 also shows the diffusion coefficient calculated from the viscosity of the Li$_2$O·2SiO$_2$ glass, Ba0 (x = 0), which was fitted by the Volger-Fulcher-Tamman (VFT) equation,

$$\eta = 2.178 \cdot 10^{-3} \exp\left(\frac{7903.7}{T - 490}\right)[\text{Pa} \cdot \text{s}], \qquad (24)$$

taking into account the Stokes—Einstein-Eyring relationship,

$$D_\eta = \frac{k_B T}{d_0 \eta} \qquad (25)$$

with $d_0 = 0.2$nm. This value of d_0 is similar to the Si—O distance, and was fitted to match the D_η with D_U at high temperatures.

The overlap of temperature intervals for D_U and D for glass Ba0 (x = 0) enables us to state with certainty that at low temperatures the $D_U(T)$ are significantly higher than $D(T)$. Therefore, we can conclude that the growth rate of nano-crystals is lower than that of macro-crystals. This result corroborates reported studies [37—39], where the growth of macroscopic crystals was preceded by a long period (see, e.g., Fig. 14a) of a very slow growth of the nanosized
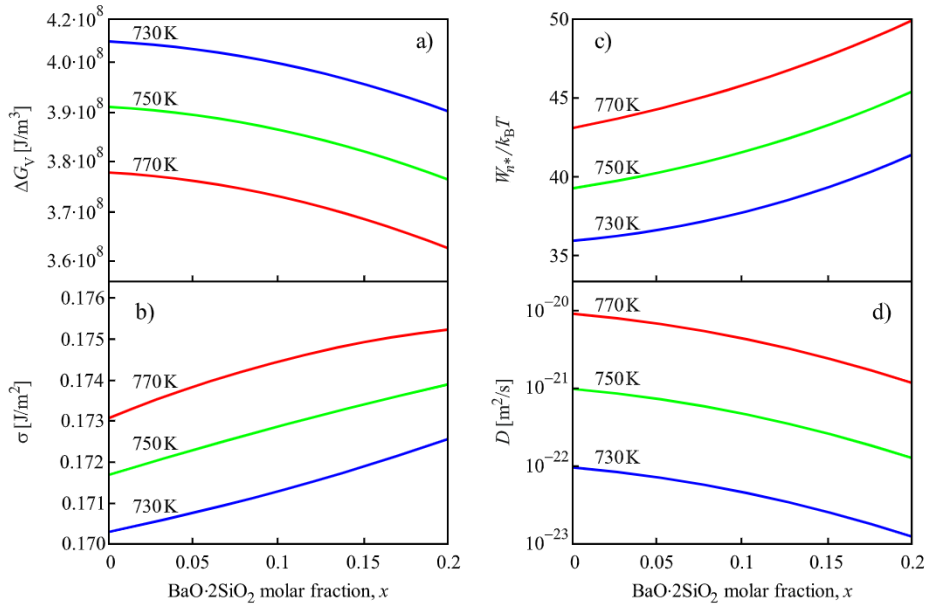
Fig. 12. a) Driving force of crystallization, ΔG_V, b) surface energy, σ, c) thermodynamic barrier W_{n^*}, and d) diffusion coefficient D determined by Eqs. ((1), (10), (20) and (21), respectively, versus glass composition, x, for different temperatures in the temperature range near the nucleation maximum.
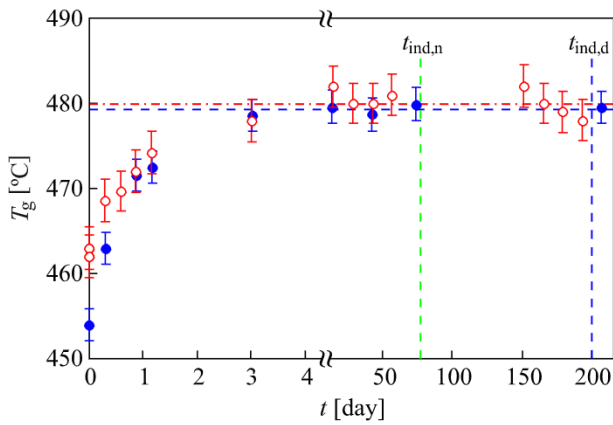

Fig. 13. Glass transition temperature $T_g(t)$ estimated by DSC for the Ba20 glass as a function of annealing time at $T = 415°C$ (40–45 °C below the initial T_g). The hollow and solid points correspond to samples pre-annealed for 3 h at $T = 430$ °C and splat cooled glasses, respectively. It takes only 3–4 days to relax fully, whereas the estimated time to form the first critical nucleus is $t_1 = $ **25** days.

crystals. This unsolved problem warrants further investigation.

The comparison of crystal nucleation and growth kinetics shows that the effect of composition on growth rates is much weaker than on the nucleation rates since the latter is determined mainly by changing the thermodynamic barrier, which is negligible in the case of crystal growth.

4.2.4. Diffusion zones and formation of a second phase

The growth of lithium disilicate crystals in glasses Ba10 and Ba20 leads to the formation of diffusion zones enriched in barium. These zones are located mainly between the branches of the dendritic lithium disilicate crystals, and are brighter than the glass region far from the crystals, as seen in the SEM BSE image of a partially crystallized glass Ba10, Fig. 16. The composition of diffusion zones must approach the eutectic one. Thus, the average composition of the crystal and its diffusion zone must be close to the composition of the original glass. At an advanced stage of the
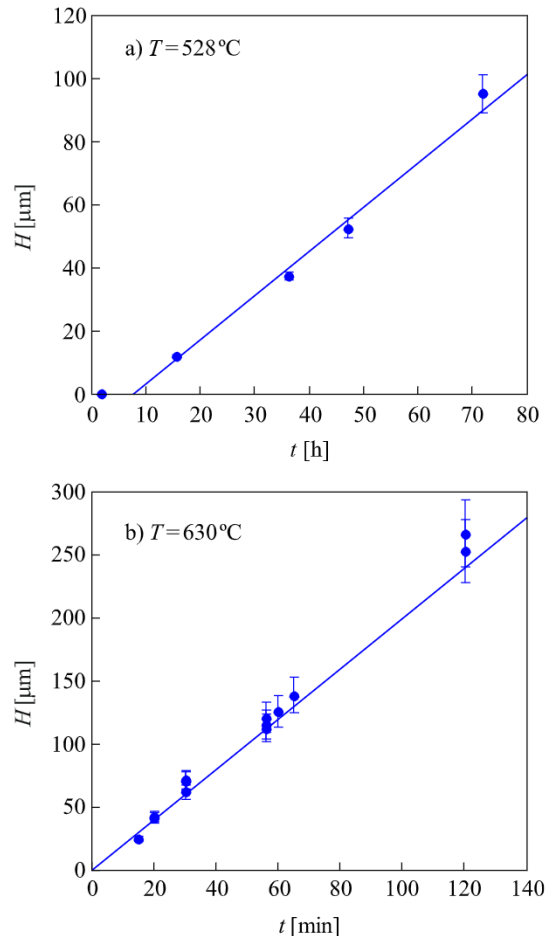

Fig. 14. Maximum crystal size, H, versus time at two growth temperatures, 528 °C and 630 °C, for the Ba20 glass.
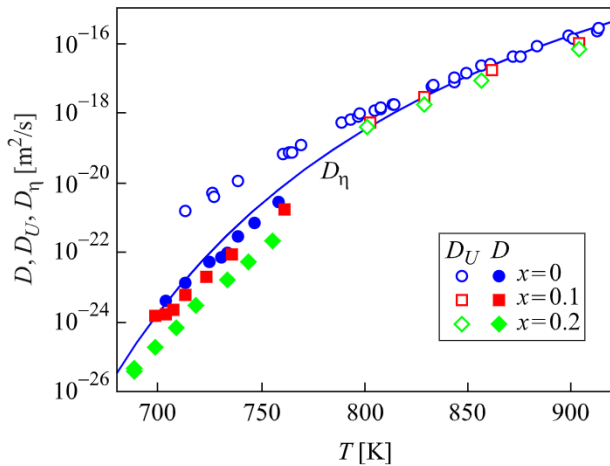
Fig. 15. Diffusivities computed from the experimental $N(t)$ plots, D, and from the growth rates of macroscopic crystals, D_U, via Eq. (22), for different BaO·2SiO$_2$ molar fractions, x, as a function of the temperature. The continuous line shows the diffusion coefficient calculated from the viscosity of the Ba0 glass, D_η.
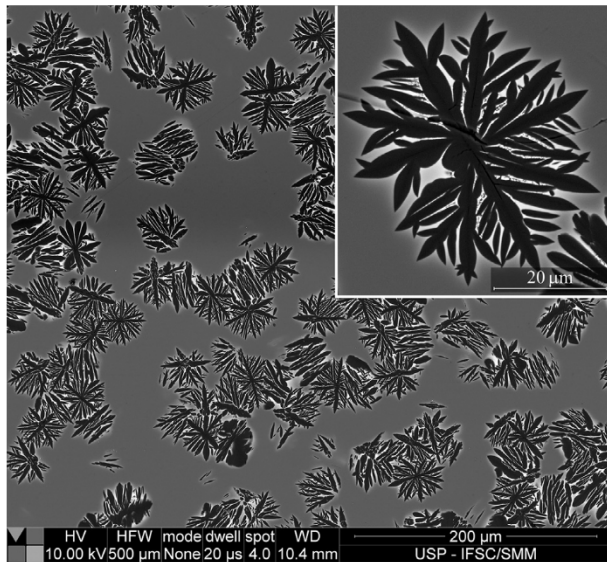

Fig. 17. SEM-BSE image of a cross-section of glass sample (Ba20) treated at $T_n = 460\,^\circ C$ for 18 h, and $T_d = 636\,^\circ C$ for 11 min. The dark areas refer to branches of the lithium disilicate dendrites, between which the crystallization product of the diffusion zone appears, consisting of interleaved crystals of barium and lithium disilicates.

Fig. 16. SEM BSE image of a cross-section of glass sample (Ba10) treated at $T_n = 462\,^\circ C$ for 1070 min, and $T_d = 636\,^\circ C$ for 11 min.

Fig. 18. SEM image of a cross-section of a fully crystallized glass sample (Ba20) nucleated at $T_n = 460\,^\circ C$ for 72 h and developed at $T_d = 630\,^\circ C$ for 120 min. The inset is a zoom of the marked area.

phase transition, these zones crystallize with a eutectic morphology, which is a regular permeation of lath-shaped crystals of barium and lithium disilicates. Crystallization in the diffusion zones of glass Ba20 occurs at an earlier stage than in glass Ba10 (Fig. 17).

Fig. 18 shows a fully crystallized sample of Ba20 glass including large primary crystals of lithium disilicate and fine-crystalline regions consisting of alternating crystals of lithium and barium disilicates, zoomed in the inset (see also X-ray diffraction spectra in Fig. 7b).

The combination of dendritic crystallization of lithium disilicate with the eutectic crystallization of the diffusion zones is also seen for the Ba30 glass, which crystallizes only from the surface (Fig. 19).

Based on the data presented in this section, we can conclude that after crystallization of the primary phase, Li$_2$O·2SiO$_2$, barium and lithium disilicate crystals form together by crystallization in the diffusion zones, whose composition is close to the eutectic.
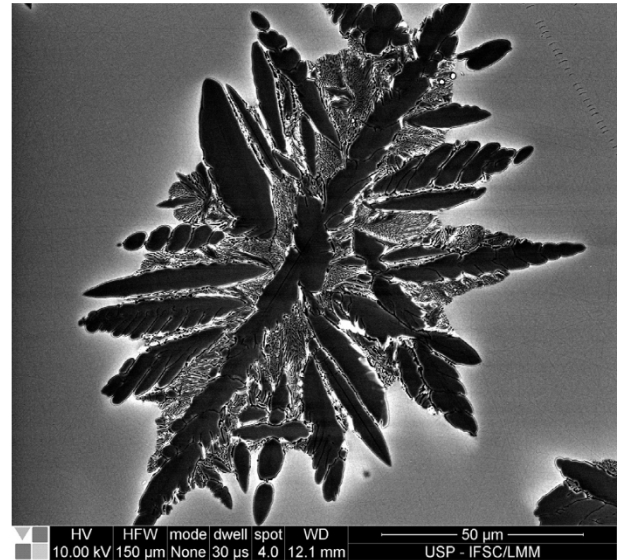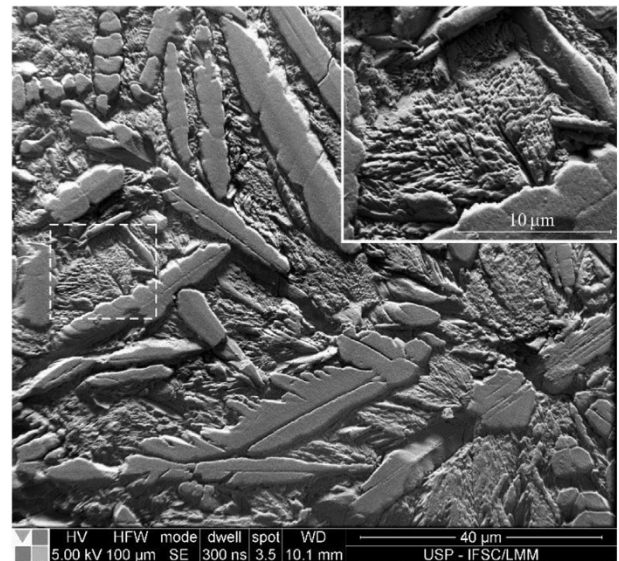
5. Summary and conclusions

We systematically studied the effect of the departure of the glass composition from the crystal stoichiometry on the crystal nucleation and growth kinetics of glasses of the pseudo-binary Li$_2$O·2SiO$_2$ − BaO·2SiO$_2$ join. A kinetic model of nucleation was used to determine a *cluster distribution function*, the steady-state nucleation rates, and induction periods for nucleation by a two-parameter fitting procedure using the experimental time dependences of the number of lithium disilicate crystals at several temperatures.

We observed that as the glass compositions depart from stoichiometry and approach the eutectic, the nucleation rates
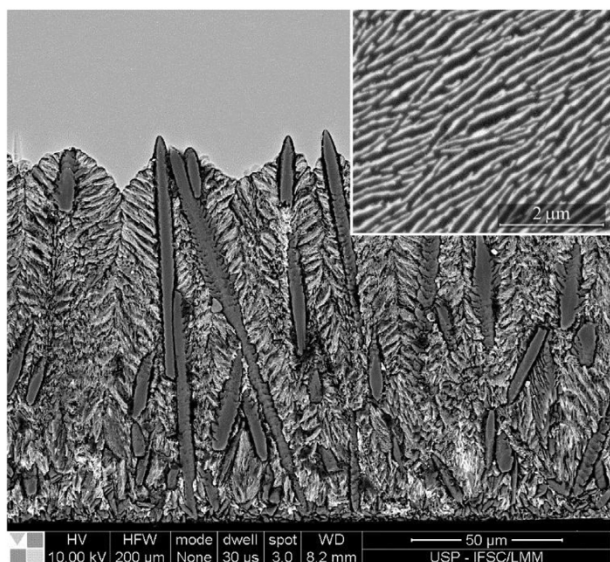
Fig. 19. SEM-BSE image of a cross-section of glass-sample (Ba30) treated at 660 °C for 30 min. The darker areas refer to the main axes of the lithium disilicate dendrites nucleated on the sample surface. The inset shows the eutectic structure formed during the crystallization of the residual glass, where the dark and light areas refer to lithium and barium disilicate crystals, respectively.

drastically drop. This is mainly due to an increase in the interfacial energy, which results in an increased thermodynamic barrier. This result corroborates the well-known fact that eutectic compositions have a good glass-forming ability.

The structural relaxation time, estimated by the evolution of the glass transition temperature during annealing, is significantly shorter than the characteristic nucleation times at the same temperature and agrees with the widely used, but scarcely tested assumption that relaxation does not affect the crystal nucleation.

For the stoichiometric glass $Li_2O \cdot 2SiO_2$, the effective diffusion coefficient determining nucleation, D, is lower than D_U determined from the growth of macroscopic crystals, and this difference significantly increases with decreasing temperature. The diffusion coefficient calculated from viscosity via the Stokes-Einstein-Eirying equation, D_η, is close to D_U at high temperatures and approaches D at low temperatures, in the glass transition range, where homogeneous nucleation rates become measurable.

Finally, after crystallization of the primary phase (lithium disilicate), barium disilicate and lithium disilicate crystals precipitate in the diffusion zones of the residual glass, whose composition is close to the eutectic. Our results shed light on the crystallization mechanism and kinetics of these non-stoichiometric glasses.

Acknowledgments

Appendix A. Supplementary data

Supplementary data to this article can be found online at https://doi.org/10.1016/j.actamat.2019.09.017.

References

[1] V.M. Fokin, G.P. Souza, E.D. Zanotto, Sodium fluoride solubility and crystallization in photo-thermo-refractive glass, J. Am. Ceram. Soc. 93 (3) (2010) 716–721, https://doi.org/10.1111/j.1551-2916.2009.03478.

[2] C. Rüssel, C. Bocker, M. Stoica, K. Thieme, A. Keshavarzi, News from glass crystallization, Journal of Chemical Technology and Metallurgy 50 (4) (2015) 357–366.

[3] C.M. Rodrigues, G.T. Niitsu, E.D. Zanotto, M.O. Prado, V. Fokin, Crystallization kinetics of 1Na2O ·2CaO·3SiO2 glass monitored by electrical conductivity measurements, J. Non-Cryst. Solids 353 (2007) 2237–2243, https://doi.org/10.1016/j.jnoncrysol.2007.03.015.

[4] R.B. Nuernberg, T.S. Bello, V.M. Fokin, E.D. Zanotto, A.C.M. Rodrigues, Non-stoichiometric crystallization of Li2SiO3-CaSiO3 glasses: residual glass composition from ionic conductivity, J. Non-Cryst. Solids 510 (2019) 158–165. https://doi.org/10.1016/j.jnoncrysol.2019.01.022.

[5] V.M. Fokin, R.M.C.V. Reis, A.S. Abyzov, C.R. Chinaglia, J.W.P. Schmelzer, E.D. Zanotto, Non-stoichiometric crystallization of lithium metasilicate–calcium metasilicate glasses. Part 2 — effect of the residual liquid, J. Non-Cryst. Solids 379 (2013) 131–144. https://doi.org/10.1016/j.jnoncrysol.2013.08.006.

[6] Z. Strnad, R.W. Douglas, Nucleation and crystallization in the soda-lime-silica system, Phys. Chem. Glasses 14 (2 April 1973) 33–36.

[7] C.J.R. Gonzalez-Oliver, Crystal Nucleation and Growth in Soda-Lime-Silica Glasses, the University of Sheffield, Sheffield, 1979. Ph.D. Thesis.

[8] K. Lakshmi Narayan, K.F. Kelton, First measurements of time-dependent nucleation as a function of composition in Na2O·2CaO·3SiO2 glasses, J. Non-Cryst. Solids 200 (1997) 222–230. https://doi.org/10.1016/S0022-3093(97)00276-7.

[9] E.G. Rowlands, P.F. James, Nucleation and crystal growth in the lithia-baria-silica system, in: Proc. Int. Congr. Glass, Volume 2. Extended Abstracts, Edinburgh, Scotland, 1–6 July, 2001.

[10] V.M. Fokin, O.V. Potapov, E.D. Zanotto, F.M. Spiandorello, V.L. Ugolkov, B.Z. Pevzner, Mutant crystals in Na2O· 2CaO·3SiO2 glasses, J. Non-Cryst. Solids 331 (2003) 240–253, https://doi.org/10.1016/j.jnoncrysol.2003.08.074.

[11] V.M. Fokin, N.S. Yuritsyn, O.V. Potapov, B.A. Shakhmatkin, N.M. Vedishcheva, V.L. Ugolkov, A.G. Cherepova, Nucleation of crystals in lithium-silicate glasses, Russ. J. Phys. Chem. 77 (Suppl. 1) (2003) 146–148.

[12] V.M. Fokin, E.D. Zanotto, Continuous compositional changes of crystal and liquid during crystallization of a sodium calcium silicate glass, J. Non-Cryst. Solids 353 (2007) 2459–2468, https://doi.org/10.1016/j.jnoncrysol.2007.04.014.

[13] N.S. Yuritsyn, Nucleation of crystals in sodium calcium silicate glasses of the metasilicate section, Glass Phys. Chem. 41 (1) (2015) 112–115, https://doi.org/10.1134/S1087659615010253.

[14] R. Becker, W. Doring, Kinetische behandlung der Keimbildung in übersättigten dämpfen, Ann. d. Physik 5 24 (1935) 719. https://doi.org/10.1002/andp.19354160806.

[15] R. Becker, Die Keimbildung bei der Ausscheidung in metallischen Mischkristallen, Ann. Phys. 32 (1938) 128. https://doi.org/10.1002/andp.19384240115.

[16] J. Frenkel, Kinetic Theory of Liquids, Oxford University Press, Oxford, 1946.

[17] K.F. Kelton, Numerical model for isothermal and non-isothermal crystallization of liquids and glasses, J. Non-Cryst. Solids 163 (1993) 283–296. https://doi.org/10.1016/0022-3093(93)91306-N.

[18] Von A. Dietzel, H. Wickert, N. Köppen, Zustandsdiagramm des systems Li2O-BaO-SiO2, Glastechn. Ber. 27 (1954) 147–151.

[19] V.M. Fokin, E.D. Zanotto, N.S. Yuritsyn, J.W.P. Schmelzer, Homogeneous crystal nucleation in silicate glasses: a 40 years perspective, J. Non-Cryst. Solids 352 (2006) 2681–2714, https://doi.org/10.1016/j.jnoncrysol.2006.02.074.

[20] C.V. Thompson, F. Spaepen, Homogeneous crystal nucleation in binary metallic melts, Acta Metall. 31 (1983) 2021–2027. https://doi.org/10.1016/0001-6160(83)90019-6.

[21] A.S. Abyzov, V.M. Fokin, A.M. Rodrigues, E.D. Zanotto, J.W.P. Schmelzer, The effect of elastic stresses on the thermodynamic barrier for crystal nucleation, J. Non-Cryst. Solids 432 (2016) 325–333. https://doi.org/10.1016/j.jnoncrysol.2015.10.029.

[22] K. Takahashi, T. Yoshio, Thermodynamic quantities of alkali silicates in the temperature range from 25°C to melting point, Yogyo-Kyokai-Shi 81 (1973) 524–533.

[23] J.W. Gibbs, On the equilibrium of heterogeneous substances, Transactions Connecticut Academy of Sciences 3 (108) (1875−78) 343, see also: J. W. Gibbs, The Collected Works, vol. 1, Thermodynamics (Longmans & Green, New York−London−Toronto, 1928).

[24] A.S. Abyzov, V. M. Fokin, A. M. Rodrigues, E. D. Zanotto, Nucleation model for cluster formation for the analysis of nucleation data (In preparation).

[25] D. Turnbull, J.C. Fisher, Rate of nucleation in condensed systems, J. Chem. Phys. 17 (1949) 71. https://doi.org/10.1063/1.1747055.

[26] B.E. Wyslouzil, G. Wilemski, Binary nucleation kinetics. II. Numerical solution of the birth-death equations, J. Chem. Phys. 103 (1995) 1137–1151. https://doi.org/10.1063/1.469824.

[27] M.J. Davis, Effect of the growth treatment on two-stage nucleation

experiments, J. Am. Ceram. Soc. 84 (3) (2001), https://doi.org/10.1111/j.1151-2916.2001.tb00688.x, 492–96.

[28] F. Spaepen, Homogeneous nucleation and the temperature dependence of the crystal-melt interfacial tension, in: H. Ehrenreich, D. Turnbull (Eds.), Solid State Physics, Academic Press, New York, 1994, pp. 1–32. https://doi.org/10.1016/S0081-1947(08)60638-4.

[29] L. Gránásy, Diffuse interface theory of nucleation, J. Non-Cryst. Sol. 162 (1993) 301–303. https://doi.org/10.1016/0022-3093(93)91250-7.

[30] L. Gránásy, Diffuse interface model of crystal nucleation, J. Non-Cryst. Sol. 219 (1997) 49–56. https://doi.org/10.1016/S0022-3093(97)00250-0.

[31] K.F. Kelton, A.L. Greer, Nucleation in Condensed Matter-Applications in Materials and Biology, Elsevier, Amsterdam, 2010, https://doi.org/10.1016/S1470-1804(09)01504-1.

[32] V.M. Fokin, A.S. Abyzov, E.D. Zanotto, D.R. Cassar, A.M. Rodrigues, J.W.P. Schmelzer, Crystal nucleation in glass-forming liquids: variation of the size of the "structural units" with temperature, J. Non-Cryst. Solids 447 (2016) 35–44. https://doi.org/10.1016/j.jnoncrysol.2016.05.017.

[33] A.S. Abyzov, V.M. Fokin, N.S. Yuritsyn, A.M. Rodrigues, J.W.P. Schmelzer, The effect of heterogeneous structure of glass-forming liquids on crystal nucleation, J. Non-Cryst. Solids 462 (2017) 32–40. https://doi.org/10.1016/j.jnoncrysol.2017.02.004.

[34] P.K. Gupta, D.R. Cassar, E.D. Zanotto, Role of dynamic heterogeneities in crystal nucleation kinetics in an oxide supercooled liquid, J. Chem. Phys. 145 (2016), 211920/1–211920/8, https://doi.org/10.1063/1.4964674.

[35] A.S. Abyzov, V.M. Fokin, E.D. Zanotto, Predicting homogeneous nucleation rates in silicate glass-formers, J. Non-Cryst. Solids 500 (2018) 231–234. https://doi.org/10.1016/j.jnoncrysol.2018.08.002.

[36] J.W. Christian, The Theory of Transformations in Metals and Alloys, Part I Pergamon, Oxford, 1981.

[37] J. Deubener, R. Brückner, M. Sternitzke, Induction time analysis of nucleation and crystal growth in di- and metasilicate glasses, J. Non-Cryst. Solids 163 (1993) 1–12. https://doi.org/10.1016/0022-3093(93)90638-E.

[38] V.M. Fokin, J.W.P. Schmelzer, M.L.F. Nascimento, E.D. Zanotto, Diffusion coefficients for crystal nucleation and growth in deeply undercooled glass-forming liquids, J. Chem. Phys. 126 (2007) 234507, https://doi.org/10.1063/1.2746502.

[39] V.M. Fokin, N.S. Yuritsyn, E.D. Zanotto, J.W.P. Schmelzer, A.A. Cabral, Nucleation time-lag from nucleation and growth experiments in deeply undercooled glass-forming liquids, J. Non-Cryst. Solids 354 (2008) 3785–3792, https://doi.org/10.1016/j.jnoncrysol.2008.05.011.